Extending *ab initio* simulations for the ion-ion structure factor of warm dense aluminum to the hydrodynamic limit using neural network potentials

Maximilian Schörner,[1] Hannes R. Rüter,[2] Martin French,[1] and Ronald Redmer[1]
[1]*Universität Rostock, Institut für Physik, D-18051 Rostock, Germany*
[2]*CFisUC, Department of Physics, University of Coimbra, Coimbra, 3004-516, Portugal*

(Received 1 March 2022; revised 5 May 2022; accepted 19 May 2022; published 31 May 2022)

We calculate the intermediate scattering function of warm dense aluminum by using density functional theory molecular dynamics simulations. From this data set, we derive the static and dynamic ion-ion structure factors. By applying a generalized collective modes model, we can fit the excitation spectra of the ion system and thereby extract the dispersion for the ion acoustic modes, as well as the decay coefficients for the diffusive and collective modes. The results are discussed and compared with experimental data if available. We show that computational limitations prevent sufficient access to the hydrodynamic limit and demonstrate that this can be circumvented using high-dimensional neural network potentials. We extract the ionic thermal conductivity of aluminum in the hydrodynamic limit and compare to values computed using a Green-Kubo relation. We highlight the importance of partitioning the heat capacity into electronic and ionic contributions and only using the ionic contribution to compute the thermal conductivity of the ions in the hydrodynamic limit.

DOI: 10.1103/PhysRevB.105.174310

I. INTRODUCTION

The theoretical description of dense Coulomb systems poses many challenges. The long-range character of the Coulomb interaction leads to many-particle effects such as dynamic screening and self-energy, which modify the effective interactions and, thereby, also the dispersion relations and excitation spectra dramatically compared with dilute, weakly interacting systems. Methods which rely on expansions with respect to small parameters (e.g., virial, activity, fugacity expansions) are not applicable. Furthermore, a quantum treatment has to be applied in order to incorporate Heisenberg's uncertainty principle and Pauli's exclusion principle present in fermionic systems. Such quantum statistical descriptions have been developed successfully for dense plasmas based on, e.g., Green's functions [1,2] and integral equations [3]. Their calculation is, however, complicated since a hierarchy for the equations of motion or the correlation functions follows which has to be truncated on an appropriate level, see Ref. [4].

For the description of warm dense matter (WDM), i.e., plasmas at high densities as typical for condensed matter and temperatures of only few eV, the quantum and correlation effects are dominant. Interestingly, the interior of planets can be mapped to the WDM region and corresponding data for the equation of state and the transport coefficients are crucial for models of their interior structure (e.g., core and mantle for rocky planets [5] or core and fluid envelopes of different composition for giant planets [6,7]), their thermal evolution (cooling behavior) [8,9] and magnetic field generation (dynamo action) [10,11]. However, the determination of equation of state data and, in particular, of transport coefficients of WDM via shock wave or ramp compression experiments is complicated so that reliable theoretical predictions are indispensible.

Therefore methods of condensed matter physics were transferred successfully to this state, located between conventional condensed matter and high-temperature plasmas. [12] A very efficient method is based on electronic structure calculations using density functional theory (DFT) for a given configuration of nuclei. The results are in turn used to compute the forces on the nuclei via the Hellmann-Feynman theorem so that they can be propagated in a molecular dynamics (MD) step. The repeated cycling through this scheme is known as DFT-MD method, which yields accurate structural properties, equation of state data, and transport coefficients of WDM, see Refs. [12,13].

As the DFT-MD calculations describe the evolution of the system in time, dynamic properties of WDM can also be computed through space- and time-dependent correlation functions. In the limit of large length and time scales it is possible to average out the effects of individual particles, which leads to the hydrodynamic description. A fundamental problem in this context are the large scales that must be realized for a standard hydrodynamic description [14] to remain valid in WDM. One of the most prominent extensions of this description to higher wave numbers is named generalized hydrodynamics [15,16], or the more general generalized collective mode (GCM) approach. [17] Many principal studies on model systems like the Yukawa one-component plasma [18,19] and the generalized Lennard-Jones system [20] developed techniques to analyze MD results in this regime. Early numerical descriptions of real systems used classical MD simulations with respect to effective quantum potentials [21,22]. However, it is an open question whether or not the dynamic properties of a dense, interacting quantum system

can properly be described by effective two-particle potentials. This is no limitation in DFT-MD calculations due to their self-consistent many-body nature.

An orbital-free (OF) formulation of DFT was used to compute the dynamic ion-ion structure factor for warm dense aluminum [23]. Although no effective pair potentials were used, the OF approach lacks the explicit formulation with discrete Kohn-Sham orbitals, which is especially important in dense systems that differ significantly from a free-electron-gas-like system and exhibit condensed matter characteristics. Much more expensive DFT-MD simulations within a full Kohn-Sham treatment were performed in a previous paper for liquid and warm dense aluminum [24], which should emulate the forces on the ions adequately. As a result the ion-acoustic modes were resolved and their dispersion relations given. This approach has also been used successfully for warm dense lithium [25]. Recently, deep potential molecular dynamics simulations [26] and molecular dynamics simulation employing ion-ion potentials constructed from a neutral pseudoatom model [27] were used to study the nonequilibrium effects of two-temperature warm dense aluminum, which was shown to be present in laser-shocked aluminum [28]. The latter two methods are computationally significantly less expensive than DFT-MD simulations and therefore enable large-scale simulations with more than 100 000 atoms, which makes the hydrodynamic regime better accessible. We adopt a similar approach as Ref. [26], in the following called neural network molecular dynamics (NN-MD), to extend our DFT-MD simulations to larger scales by using high-dimensional neural network potentials implemented in the N2P2 software package, [29–31] which employs Behler-Parrinello symmetry functions [32].

In the present paper we apply the method presented in Ref. [24] in order to calculate the dynamic ion-ion structure factor in warm dense aluminum for a wider range of parameters (density, temperature), see Sec. II. We give a brief overview of the error analysis in Sec. III and compare the static and dynamic structure factor with available experimental results in Sec. IV. Furthermore, we fit the numerical data for the dynamic structure factor (DSF) to a generalized hydrodynamic model in Sec. V and derive dispersion relations and the decay coefficients. Here, we compare the capability of extracting thermodynamic and transport properties, in particular, the thermal conductvity of the ions, in the hydrodynamic limit between the NN-MD and the DFT-MD simulations. In principle, highly resolved measurements of the ion-ion DSF for WDM states would enable the determination of these quantities for such extreme condition. Corresponding inelastic x-ray scattering experiments are planned at free electron laser facilities like the European XFEL [33,34] or the LCLS in Stanford [35]. At the end, we give conclusions in Sec. VI.

II. THEORETICAL METHOD

Although DFT-MD allows access to information on both the electronic and ionic system, all quantities of interest in this paper can be derived from the ion positions at each point in time. From this the ion-ion intermediate scattering function

$$F_{\mathrm{ii}}(\vec{k},t) := \frac{1}{N}\left\langle n^{(\mathrm{i})}_{\vec{k}}(\tau)\, n^{(\mathrm{i})}_{-\vec{k}}(\tau+t)\right\rangle_{\tau}, \tag{1}$$

with

$$\langle \dots \rangle_{\tau} = \lim_{\Theta\to\infty} \frac{1}{\Theta}\int_0^{\Theta} \dots \, d\tau \tag{2}$$

can be determined where $n^{(\mathrm{i})}_{\vec{k}}(t) = \sum_{i=1}^{N} \mathrm{e}^{-\mathrm{i}\vec{k}\cdot\vec{r}_i(t)}$ is the Fourier transformed ion number density and $\vec{k}$ is the wave vector. The number of ions is denoted by N and Θ is the simulation duration, which must approach infinity in the exact relation. We approximate this limit by sufficiently long simulation times.

The dynamic ion-ion structure factor $S_{\mathrm{ii}}(\vec{k},\omega)$ is given by the Fourier transform of the intermediate scattering function

$$S_{\mathrm{ii}}(\vec{k},\omega) := \frac{1}{2\pi}\int_{-\infty}^{\infty} F_{\mathrm{ii}}(\vec{k},t) e^{i\omega t} dt, \tag{3}$$

with the angular frequency ω. By virtue of the Wiener-Khinchin theorem this is equivalent to

$$S_{\mathrm{ii}}(\vec{k},\omega) = \lim_{\Theta\to\infty} \frac{1}{2\pi N\Theta}\left|\int_{-\Theta/2}^{\Theta/2} n^{(\mathrm{i})}_{\vec{k}}(t) e^{i\omega t} dt\right|^2, \tag{4}$$

which is the formula we employed for the present calculations. The intermediate scattering function $F_{\mathrm{ii}}(\vec{k},t)$ is then determined by an inverse Fourier transformation of $S_{\mathrm{ii}}(\vec{k},\omega)$. Analogously, the longitudinal and transverse current spectra can be determined from

$$J_{\mathrm{ii,l/t}}(\vec{k},\omega) := \lim_{\Theta\to\infty} \frac{1}{2\pi N\Theta}\left|\int_{-\Theta/2}^{\Theta/2} j^{(\mathrm{i,l/t})}_{\vec{k}}(t) e^{i\omega t} dt\right|^2, \tag{5}$$

and

$$j^{(\mathrm{i,l})}_{\vec{k}}(t) = \sum_{i=1}^{N} v_i^{\parallel}\, \mathrm{e}^{-\mathrm{i}\vec{k}\cdot\vec{r}_i(t)}, \tag{6}$$

$$j^{(\mathrm{i,t})}_{\vec{k}}(t) = \sum_{i=1}^{N} v_i^{\perp}\, \mathrm{e}^{-\mathrm{i}\vec{k}\cdot\vec{r}_i(t)}, \tag{7}$$

where $v_i^{\parallel}$ is the component of the velocity which is parallel to $\vec{k}$, and $v_i^{\perp}$ is the component which is parallel to a given $\vec{k}_{\perp}$, which is perpendicular to $\vec{k}$. Velocities are computed from the ion positions via central finite differences. The shape of the simulation box determines the wave vectors $\vec{k}$ at which $S_{\mathrm{ii}}(\vec{k},\omega)$ can be evaluated. Only wave vectors that result in complete oscillations within the simulation box are allowed and can be computed from the reciprocal lattice vectors.

The ion dynamics are obtained by performing DFT-MD simulations with the Vienna *ab initio* simulation package (VASP) [36–38]. Within these simulations the Born-Oppenheimer approximation is used to decouple the ion and electron dynamics. For the determination of the electron density the finite temperature DFT approach [39] is used, employing the generalized gradient approximation of Perdew, Burke, and Ernzerhof [40] for the exchange correlation functional. At each time step the electron density is determined self-consistently, which allows the determination of the forces acting on each ion. The ions are moved classically due to the Coulomb interactions with the other ions and the electrons by solving Newton's second law for a given time step Δt. Within the VASP code the electronic wave functions are expanded into plane waves up to a cutoff energy E_{cut} and

TABLE I. Overview of the simulation parameters used in this study: temperature T, mass density ρ, size of time step Δt, number of ions in DFT-MD simulation $N_\mathrm{i}^\mathrm{DFT}$ and number of ions in NN-MD simulation N_i^NN.

T [K]	$k_\mathrm{B}T$ (eV)	ρ (g/cm^3)	Δt (fs)	$N_\mathrm{i}^\mathrm{DFT}$	N_i^NN
1000	0.086	2.356	3.0	125	32 000
5802	0.5	2.356	1.0	125	32 000
5802	0.5	4.712	1.0	125	32 000
11605	1.0	2.356	1.0	125	32 000
11605	1.0	4.712	1.0	125	32 000
58023	5.0	4.712	1.0	125	32 000
58023	5.0	8.1	1.0	125	32 000

projector augmented-wave potentials [41] are used to describe the ion potential. For aluminum we employ the PAW PBE Al 04Jan2001 potential, which treats the ten inner electrons within a frozen core approximation and only considers the three valence electrons within the DFT framework. We use a cutoff energy of 700 eV. For the temperature control the algorithm of Nosé-Hoover [42,43] is used with a mass parameter corresponding to a temperature oscillation period of 40 time steps. The simulation box for aluminum is spanned by vectors that correspond to its solid lattice structure: face centered cubic (fcc). The sampling of the Brillouin zone was carried out at the Baldereschi mean value point [44]. We have carefully checked the convergence of our results with regard to plane wave energy cutoff, length of the time step, number of particles and Brillouin zone sampling.

In order to enable a larger simulation size, we train a high-dimensional neural network potential, implemented in the N2P2 software package [29,30], using the energies and forces predicted by the DFT-MD simulations. Although these simulations are performed at finite electron temperature, we use an extrapolation of the internal energy to its value at zero electron temperature (provided by VASP [45]) to train the neural network. This allows us to exclude the contributions from electronic excitations to the internal energy, and, by extension, the electronic contributions to the heat capacity which we compute in Sec. V C. The neural network uses Behler-Parrinello symmetry functions [32] to describe the surrounding of each ion and employs a Kalman filter to update the network during the training procedure. We employ the default neural network configuration with a cutoff radius ranging from 4 Å for the simulations at 8.1 g/cm^3 to 6 Å at 2.356 g/cm^3. The surrounding of the ions is described by ten radial symmetry functions and twelve narrow angular symmetry functions, with parameters chosen according to Ref. [46]. The neural network potential is then used in conjunction with the classical molecular dynamics simulation code LAMMPS [47] to generate the NN-MD simulations. We train a separate neural network for each condition to ensure the highest accuracy in reproducing the DFT-MD results. The networks are trained on 10 000 configurations, which are randomly sampled from the 20 000 time steps of the DFT-MD simulation and additional 5000 time steps at slightly higher and lower temperature and density. We give the specific parameters used in the simulations in Table I. For $k_\mathrm{B}T = 0.5$ eV and $\rho = 4.712$ g/cm^3, aluminum froze into an fcc lattice, while at all other conditions it remained a liquid.

III. FITTING PROCEDURE AND ERROR ANALYSIS

A. Fit to generalized collective modes

For the DSF of liquids and plasmas, there exists a well known limiting case at long wavelength $k \to 0$ and low frequencies $\omega \to 0$, the hydrodynamic limit [21]. In this limit, the DSF consists of a zero-centered Lorentzian peak, which is called the diffusive mode, and two Lorentzian shaped side peaks, which are called propagating collective modes, centered at finite frequencies [14].

The diffusive mode is mainly determined by the thermal diffusivity, while for the collective modes also the adiabatic speed of sound and the viscosity of the medium play a role. This limiting case can be extended to a generalized hydrodynamic model, in which the general shape of the DSF is kept the same but the transport coefficients become dependent on the wave number $|\vec{k}|$. While this approach shows good results at small wave numbers, [18] especially beyond the first correlation peak, nonhydrodynamic thermal modes and structural relaxation modes also contribute to the DSF [48]. Theoretical models for the description of the DSF at a wide range of wave vectors have been developed, with the generalized collective mode (GCM) approach being one of the most successful [49]. It extends the set of considered dynamic variables from the three hydrodynamic variables particle density, energy density, and momentum density to include their derivatives or other nonconserved variables, resulting in additional mode contributions to the correlation functions. However, since these microscopic variables cannot be observed in experiments and access to the local energy density in *ab initio* simulations is restricted, several fitting as well as fit-free methods [48] have been developed.

In this paper, we adopt the fitting scheme of Wax and Bryk [50]. Within this scheme the intermediate scattering function is modeled according to a GCM approach with one propagating and one diffusive mode

$$\begin{aligned} F_\mathrm{ii}^\mathrm{GCM}(\vec{k},t) &= A\,e^{-\alpha|t|} + (B_1\cos(\omega_0|t|) \\ &\quad + B_2\sin(\omega_0|t|))\,e^{-\beta|t|} \\ &= A\,e^{-\alpha|t|} + C\cos(\omega_0|t| + \phi)\,e^{-\beta|t|}, \end{aligned} \tag{8}$$

with the relation

$$C = \sqrt{B_1^2 + B_2^2}, \quad \phi = \arctan\left(-\frac{B_2}{B_1}\right), \tag{9}$$

leading, via the Fourier transform (3), to the DSF

$$\begin{aligned} S_\mathrm{ii}^\mathrm{GCM}(\vec{k},\omega) = \frac{1}{2\pi}\Bigg(&\frac{2A\alpha}{\alpha^2+\omega^2} + \frac{B_1\beta}{\beta^2+(\omega_0+\omega)^2} \\ &+ \frac{B_1\beta}{\beta^2+(\omega_0-\omega)^2} + \frac{B_2(\omega_0+\omega)}{\beta^2+(\omega_0+\omega)^2} \\ &+ \frac{B_2(\omega_0-\omega)}{\beta^2+(\omega_0-\omega)^2}\Bigg). \end{aligned} \tag{10}$$

The zero-centered Lorentzian in Eq. (10) corresponds to a diffusive process, while the remaining Lorentzians at finite

frequencies correspond to propagating processes. These two modes are not necessarily the hydrodynamic modes, although they will coincide with them in the limit $k \to 0$. In the GCM scheme, modes correspond to either real or imaginary eigenvalues of the generalized hydrodynamic matrix, with real eigenvalues leading to diffusive modes and imaginary eigenvalues corresponding to propagating processes. Therefore, in this fitting scheme, it is assumed that the behavior of the system can be described by the two (hydrodynamic or nonhydrodynamic) modes of Eqs. (8) and (10). Similar to Ref. [50], we find that the inclusion of an additional mode does not improve the results enough to justify the addition of further fitting parameters. The parameters A, B_1, B_2, α, β, and ω_0 are unknown functions of the wave number k, but we omit the index k for brevity. Following the fitting scheme of Ref. [50], A, B_1, and B_2 can be eliminated as independent parameters by constraining the model function to obey the zeroth, first, and second frequency moments:

$$\int_{-\infty}^{\infty} S_{\mathrm{ii}}(k,\omega)\, d\omega = S_{\mathrm{ii}}(k), \tag{11}$$

$$\int_{-\infty}^{\infty} S_{\mathrm{ii}}(k,\omega)\omega\, d\omega = 0, \tag{12}$$

$$\int_{-\infty}^{\infty} S_{\mathrm{ii}}(k,\omega)\omega^2\, d\omega = -\partial_t^2 F_{\mathrm{ii}}(k,t)|_{t=0}. \tag{13}$$

The first frequency moment is constrained to be zero, therefore this model avoids the unphysical cusp in $F_{\mathrm{ii}}(\vec{k},t)$ at $t=0$ that is present in the hydrodynamic model. In contrast to Ref. [50] for the second frequency moment, we do not use the one component plasma (OCP) value, but the value directly obtained from the intermediate scattering function $F_{\mathrm{ii}}(\vec{k},t)$ by finite differences.

For curve fitting we seek to minimize the least-square merit function of the form:

$$\chi(\vec{k}) = \sum_{i=0}^{N_{\mathrm{d}}} w_i (f^{\mathrm{model}}(i) - f^{\mathrm{data}}(i))^2, \tag{14}$$

where f^{model} is a model function one tries to fit to the dataset f^{data}, N_{d} is the number of data points and w_i is the weight for the ith data point, which is usually chosen to be the inverse variance $1/\sigma^2_{f(i)}$. Following the scheme of Ref. [50], the parameters α, β and ω_0 are obtained by fitting Eqs. (8) and (10) to F_{ii} and S_{ii} obtained from the DFT-MD and NN-MD simulations. The standard deviation of each data point is determined through the error analysis described in the next section. From the Jacobian of the fitting problem (14) with respect to the fitting parameters, it is possible to estimate a standard error for these parameters. It should be pointed out that this error merely describes how sensitive the fit to the simulation data is to small changes in the respective fitting parameter. It includes no information on the physical validity of the given model function, which has to be discussed separately.

For fitting we employ a standard Marquardt-Levenberg fitting algorithm (as implemented in the SCIPY library for scientific computing in PYTHON [51]) obtaining first the parameters β and ω_0 by fitting to S_{ii} keeping α fixed. Then α is obtained by fitting to F_{ii} with β and ω_0 fixed. This procedure is then repeated until all parameters converge to an accuracy of 0.001%.

B. Error analysis

For the estimation of the errors we report the confidence intervals calculated for a confidence level of 68% (i.e., one standard deviation). Here, we follow the error estimation of Welch for the use of the Fast Fourier Transform in power spectra calculations [52]. A DSF calculated by Eq. (4) has a standard deviation of $\sigma_{S(\vec{k},\omega)} = S(\vec{k},\omega)$. By splitting the duration of the simulation into N_I intervals and averaging over all individual power spectra, the standard deviation of $S^{\mathrm{GCM}}_{\mathrm{ii}}(\vec{k},\omega)$ is reduced by $\sqrt{N_I}$. Because the systems under investigation are isotropic we report only on quantities depending on the magnitude of the wave vector $|\vec{k}|$ and averages over the N_k wave vectors with magnitude $|\vec{k}|$ can be performed. In addition, since the ions are treated classically in our simulations, we expect the intermediate scattering function $F(\vec{k},t)$ to be symmetric and real-valued, corresponding to a real and symmetric DSF with respect to ω. Therefore an average of the positive and negative frequency part is taken which results in a further reduction of the error leading to the error approximation

$$\sigma_{S_{\mathrm{ii}}(\vec{k},\omega)} \approx \frac{S_{\mathrm{ii}}(\vec{k},\omega)}{\sqrt{2N_k N_I}}. \tag{15}$$

While the number of intervals stays constant during the analysis, the number of wave vectors corresponding to a given magnitude increases with $|\vec{k}|$, causing lower relative errors at larger wave vectors.

In our calculations, we arrive at the intermediate scattering function via the Fast Fourier Transform from the DSF $S_{\mathrm{ii}}(\vec{k},\omega)$. Using quadratic error propagation on the formulation of the fast Fourier transform leads to a constant error

$$\begin{aligned}\sigma_{F_{\mathrm{ii}}(\vec{k},t)} &= \sqrt{\sum_j \sigma^2_{S_{\mathrm{ii}}(\vec{k},\omega_j)}}\,\Delta\omega \\ &\approx \sqrt{\sum_j \frac{S_{\mathrm{ii}}(\vec{k},\omega_j)^2}{2N_k N_I}}\,\Delta\omega,\end{aligned} \tag{16}$$

where ω_j are the discrete frequencies available from the Fourier transform and $\Delta\omega$ is their spacing. Using Eqs. (15) and (16) for the weight w_i in (14) allows us to extract an estimated error on the fit parameters α, β, ω, and, using error propagation on the equations given by the sum rules, also for the remaining parameters.

In order to further reduce noise in the simulation data, a window function $g_{\vec{k}}(t)$ is applied to the intermediate scattering function to suppress statistical oscillations at large times t.

IV. RESULTS FOR THE STATIC AND DYNAMIC STRUCTURE FACTOR

A. The static ion-ion structure factor

To validate the accuracy of our simulation approach, we compare with experimental x-ray diffraction data [53] available for small temperatures in Fig. 1.

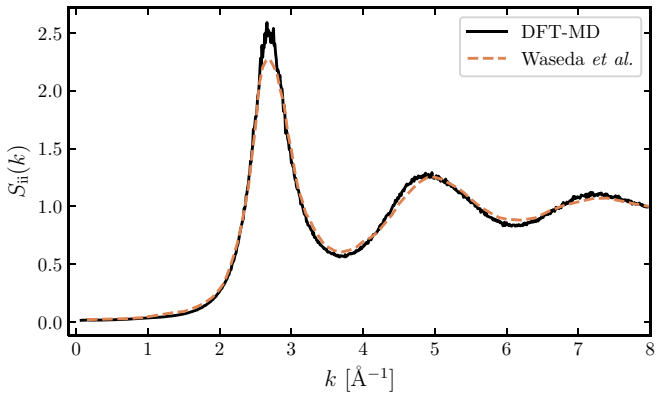

FIG. 1. Comparison of DFT-MD calculations and experimental results [53] for liquid aluminum at 2.356 g/cm^3 and $T = 1000$ K.

Very good agreement is found except for values around the first peak, where a sharp cusp is observed. A similar behavior has also been observed in earlier MD simulations, which can be explained by the periodic boundary conditions that induce additional order. Furthermore, the statistical error in this region is comparatively large because of the especially large correlation times that are present there. Additionally, we show a comparison of the static ion-ion structure factor generated from the DFT-MD and NN-MD simulations in Fig. 2. It can be observed that the static structure is reproduced well by the NN-MD simulations. For the lowest considered temperature $T = 1000$ K, the first correlation peak of the NN-MD is slightly lower than that of the original DFT-MD simulation. This is due to the diminishing impact of the periodic boundary conditions in the larger simulation box of the NN-MD simulations. The agreement for the other liquid conditions not shown in Fig. 2 is equally good, while the static structure factor of solid aluminum exhibits a strong particle number dependence.

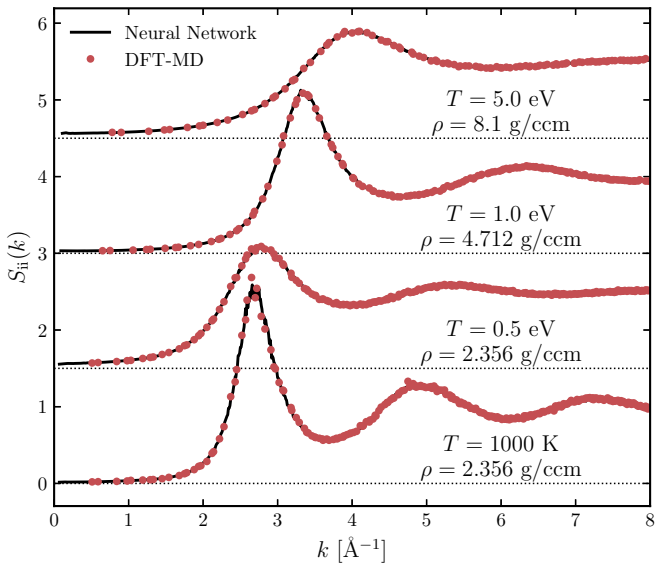

FIG. 2. Comparison of results for the static ion-ion structure factor from DFT-MD simulations and NN-MD for liquid aluminum at various conditions.

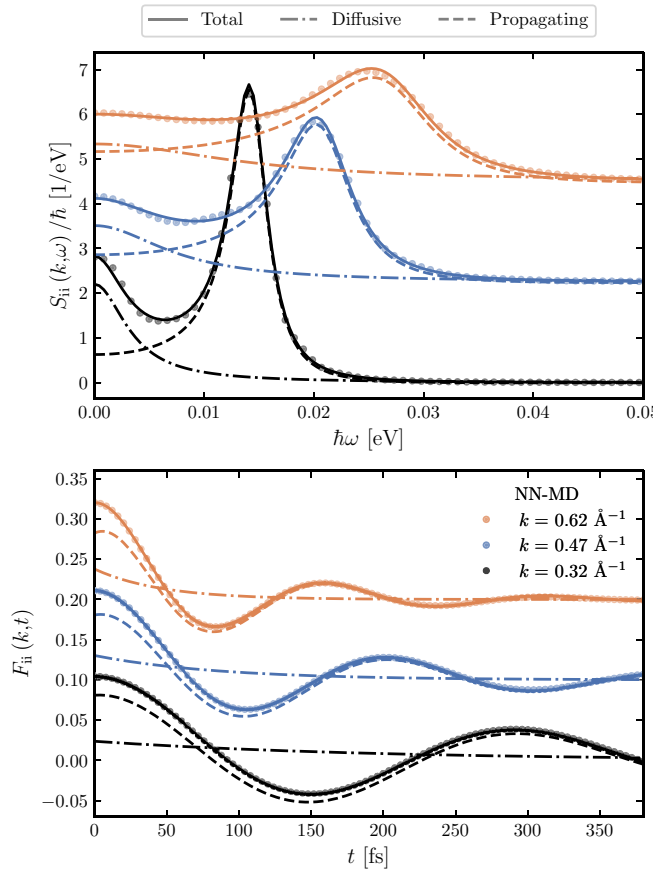

FIG. 3. Comparison of the DSF (top panel) and the intermediate scattering function (bottom panel) and the fit to the GCM model [described in Eqs. (8) and (10)] for a NN-MD simulation of aluminum at 2.356 g/cm^3 and $T = 1.0$ eV. The diffusive and propagating part of the fit are indicated separately. The curves are shifted by 2.25 eV^{-1} for the DSF and 0.1 for the intermediate scattering function with respect to each other for clarity.

B. The dynamic ion-ion structure factor

In Fig. 3, the block averaged DSF for aluminum is compared with the curves obtained by the fitting procedure at 11605 K. Very good agreement between the NN-MD data and the GCM model is found even at high wave numbers (see upper panel in Fig. 3), far from the collective region. The same observations can be made for all other conditions under investigation in this paper (Table I).

As expected, very good agreement is also found for the intermediate scattering function (see lower panel in Fig. 3). However, after the decay of the correlations, $F_{ii}(\vec{k}, t)$ exhibits statistical fluctuations at long times t. To reduce the effect of these unphysical fluctuations from the DSF and to reduce truncation effects we use a window function $g_{\vec{k}}(t)$ that is defined in terms of a decay time $\theta_{\vec{k}}$ by

$$g_{\vec{k}}(t) = \begin{cases} 1, & \text{if } |t| < \theta_{\vec{k}}/2 \\ \exp\left(-16\frac{(|t|-\theta_{\vec{k}}/2)^2}{\theta_{\vec{k}}^2}\right), & \text{if } |t| > \theta_{\vec{k}}/2 \end{cases}. \tag{17}$$

$S_{ii}(\vec{k}, \omega)$ is then obtained by Fourier transformation of $g_{\vec{k}}(t)F_{ii}(\vec{k}, t)$. The use of a window function as in Eq. (17) leaves the intermediate scattering function unchanged at

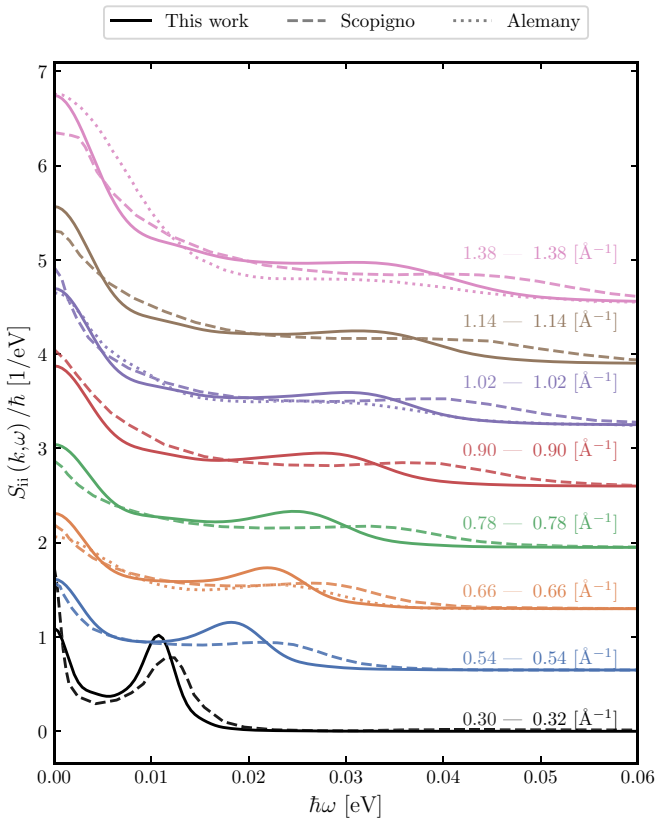

FIG. 4. DSF $S_{ii}(\vec{k},\omega)$ of liquid aluminum at $\rho = 2.356$ g/cm^3 and $T = 1000$ K. Dashed lines: experimental x-ray scattering results [54]. Dotted lines: DFT-MD of Alemany *et al.* [55]. Solid lines: present NN-MD simulations. The right wave numbers correspond to the present NN-MD results, while the left ones correspond to Refs. [54,55]. For clarity, each set of curves is shifted by an offset of 0.6 eV^{-1} with respect to the lower one.

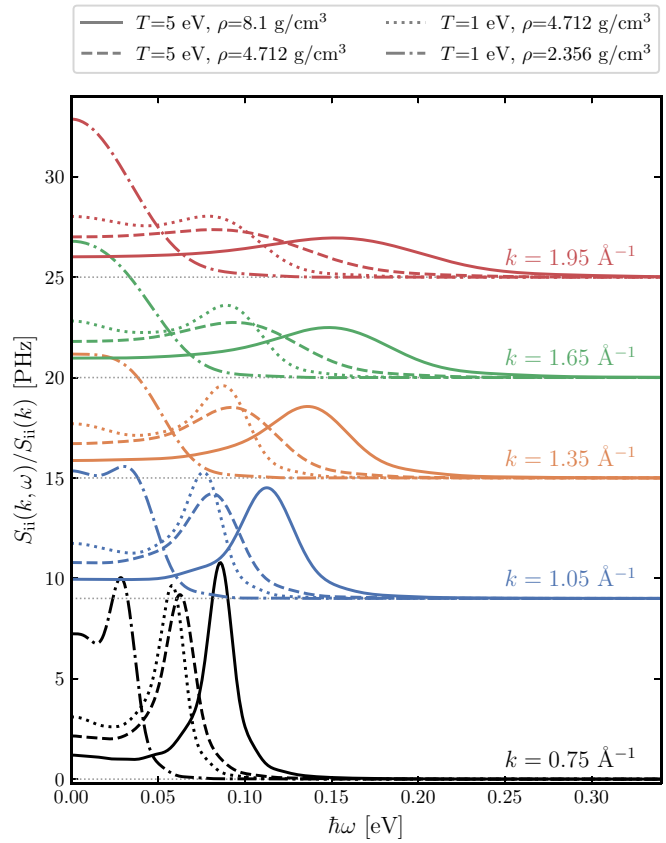

FIG. 5. DSF $S_{ii}(\vec{k},\omega)$ of warm dense aluminum at different densities and temperatures. For clarity each set of curves is shifted by an offset with respect to the lower one. The dotted lines represent the baseline for each set.

times, where statical fluctuations play a minor role, and damps the statistical fluctuations where they dominate the signal. To avoid bias in the choice of $\theta_{\vec{k}}$, it is determined from the results of the fitting procedure. We define $\theta_{\vec{k}}$ as the time after which the intermediate scattering function has decayed to 0.1% of its initial value, i.e., we use the $\theta_{\vec{k}}$ that fulfills

$$|A|e^{-\alpha\theta_{\vec{k}}} + |C|e^{-\beta\theta_{\vec{k}}} = 0.001\, F_{ii}(\vec{k},0) \tag{18}$$

$$= 0.001\,(|A| + |C|). \tag{19}$$

Note again that the fitting parameters A, C, α, and β are all wave number dependent, but the index $\vec{k}$ has been omitted. With this specific choice for the window function there are still small statistical artifacts visible in the DSF but a more important feature is that it leaves the height and form of the peaks practically unchanged.

In Fig. 4, we compare the DSF of liquid aluminum at 1000 K to several measurements of Scopigno *et al.* [54] and to earlier DFT-MD simulations [55] that used the LDA for the exchange-correlation functional. The normalization of the experimental data could not be determined from the experiment, but has been determined from fitting procedures. We found that static structure factors from this procedure are, on average, by a factor 1.52 lower than our NN-MD results and thus in Fig. 4 scaled the data of Scopigno *et al.* [54] by this factor. Alemany *et al.* [55] report on a normalized DSF $S_{ii}(\vec{k},\omega)/S_{ii}(\vec{k})$. Therefore, in Fig. 4, we scaled their data according to our $S_{ii}(\vec{k})$ for comparison. Since the calculation of the structure factor can only be carried out on the reciprocal lattice corresponding to the periodic boundary conditions, the comparison is done at those wave numbers that are closest to the ones in the experiment. Good agreement is found between our simulations and the experiment. Compared to the experiment the peaks and shoulders are located at slightly lower frequencies in our simulation and the peaks are more pronounced. Compared to the *ab initio* calculation of Alemany *et al.* [55] our simulation uses a larger energy cutoff, a larger number of ions, a smaller time step and has a longer simulation time. They used the LDA for the XC contribution, while we use the GGA by Perdew, Burke, and Ernzerhof [40]. Furthermore, due to numerical limitations at the time, the previous DFT study was performed with 205 atoms for 850 time steps, which in our experience is far too few to properly converge the width and height of the side and central peak.

Figure 5 shows the DSF $S_{ii}(\vec{k},\omega)$ of warm dense aluminum at four different conditions for various wave vectors inside the first Brillouin zone, illustrating its trends with temperature and density. With increasing densities, a shift of the propagating mode to higher frequencies and a clear separation from the diffusive mode can be observed. Additionally, the

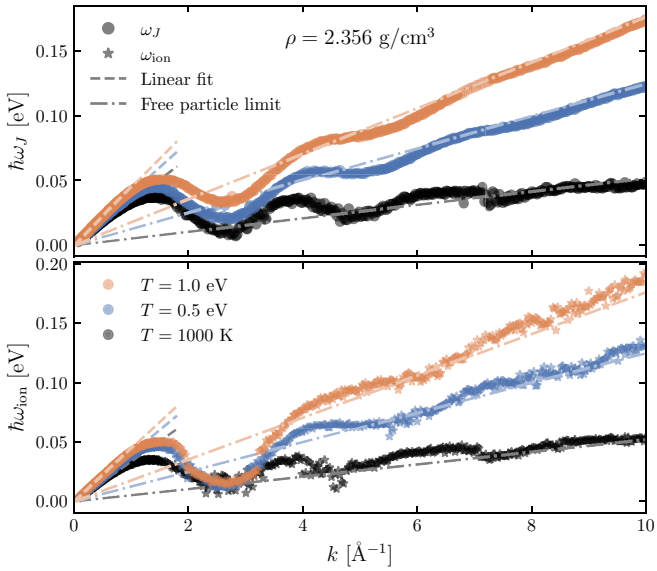

FIG. 6. Peak position ω_J of the longitudinal current-current spectral function $J_{\rm ii}(k,\omega)$ (top) and the frequency of the ion acoustic mode $\omega_{\rm ion}$ (bottom), extracted by fitting to $S_{\rm ii}(k,\omega)$, as a function of the wave number k for aluminum at various temperatures for the mass density $\rho = 2.356$ g/cm^3. The linear behavior of $\omega_{\rm ion}$ for small k, predicted by the hydrodynamic model, is indicated by dashed lines. The free particle limit of ω_J for large k is depicted by dash-dotted lines.

higher densities suppress the diffusive mode due to the higher collision rates. At constant density, a higher temperature leads to a broadening and a slight shift to higher frequencies of the propagating mode, indicating a faster sound transport in heated materials (see Sec V A).

V. MATERIAL PROPERTIES

A. Dispersion relation

The frequency $\omega_{\rm ion}$ of the ion acoustic waves can be determined from the fitting procedure, giving reliable data in the long-wavelength regime. A general quantity that does not rely on fitting is the peak position of the longitudinal current-current spectrum [see Eq. (5)], which will coincide with the hydrodynamic behavior for $k \to 0$, see Fig. 6. All investigated cases exhibit a linear dispersion at small k. At relatively low temperatures, local maxima in the peak position are observed followed by a de Gennes minimum [56] located at the position of the first correlation peak of the static structure factor $S_{\rm ii}(\vec{k})$. Analogous to the reciprocal space in solids, where the first Brillouin zone is repeated infinitely beyond its boundaries, a periodicity, albeit faster decaying, occurs in liquids due to the near-field order. At length scales characteristic of this near-field order, described by the first correlation peak, the dispersion tends back to its value at $k = 0$, similar to the dispersion of phonons going to zero at the center of neighboring Brillouin zones. This minimum becomes less pronounced for higher temperatures as the near-field order of the system decreases. Instead, the curves reach an intermediate plateau and then go over to a positive dispersion. For large k, the peak position of the longitudinal current-current spectral function

TABLE II. Adiabatic speed of sound $c_{\rm s,HD}$, extracted from the fit to the hydrodynamic model in (8) and (10) and adiabatic speed of sound $c_{\rm s,TD}$ computed from the thermodynamic relation in (22) for aluminum at given temperatures T and mass densities ρ.

T (K)	ρ (g/cm^3)	$c_{\rm s,HD}$ (km/s)	$c_{\rm s,TD}$ (km/s)
1000	2.356	5.087 ± 0.025	4.73 ± 0.12
5802	2.356	6.029 ± 0.016	6.02 ± 0.05
11 600	2.356	6.736 ± 0.018	6.73 ± 0.04
11 600	4.712	11.579 ± 0.024	11.349 ± 0.025
58 020	4.712	13.049 ± 0.017	12.908 ± 0.020
58 020	8.1	17.406 ± 0.017	17.451 ± 0.003

can be described by the classical free particle limit of a noninteracting system

$$\omega_J(\vec{k}) = \sqrt{\frac{2}{m_{\rm i}\beta}}\,|\vec{k}| \tag{20}$$

with the ion mass $m_{\rm i}$ and $1/\beta = k_{\rm B}T_{\rm i}$, where $k_{\rm B}$ is the Boltzmann constant. This peak at finite frequencies occurs because the zero-centered Gaussian DSF of a noninteracting system is multiplied by ω^2/k^2 to arrive at the longitudinal current-current spectral function. We suspect the rise of $\omega_{\rm ion}$ at high k, where the DSF is close to a perfect Gaussian, is due to our choice of fit function. Because a Gaussian cannot be approximated by a Lorentzian, a second contribution at finite frequency is necessary. This highlights the inadequacy of this fit function beyond the first correlation peak, and in the following, we will therefore not apply it there.

By fitting

$$\omega_{\rm ion}(\vec{k}) = c_s|\vec{k}| \tag{21}$$

to the small k dispersion relation of $\omega_{\rm ion}$ extracted from the fit, the adiabatic velocity of sound c_s is determined, see Table II. The dashed lines in Fig. 7 indicate the linear fit for the liquid conditions considered in this work. We use the first eight oscillation frequencies $\omega_{\rm ion}$ at each condition for the linear fit. It can be shown that the inclusion of more or less data points does not significantly impact the extracted value for the adiabatic velocity of sound. The speed of sound at 1000 K can be compared to experimental data by using the suggested best fit from Ref. [57]. For a temperature of 1000 K, one obtains a speed of sound of 4648 m/s, which is in reasonable agreement with our value of 5087 m/s. Remarkably, the experimental speed of sound is not recovered by the x-ray scattering study of Scopigno *et al.* on liquid aluminum, [54] either, from which an adiabatic speed of sound of ∼5700 m/s can be derived. Additionally, following Ref. [58] and the supplemental material of Ref. [20], we compute the adiabatic speed of sound directly from the thermodynamic relations

$$c_{\rm s,TD}^2 = \frac{1}{\rho\,\chi_S} = \frac{\gamma}{\rho\,\chi_T}, \tag{22}$$

$$\chi_T = \frac{1}{\rho}\left(\frac{\partial\rho}{\partial P}\right)_T, \tag{23}$$

with the heat capacity ratio $\gamma = C_P/C_V$, the mass density ρ, the pressure P and the adiabatic and isothermal compress-

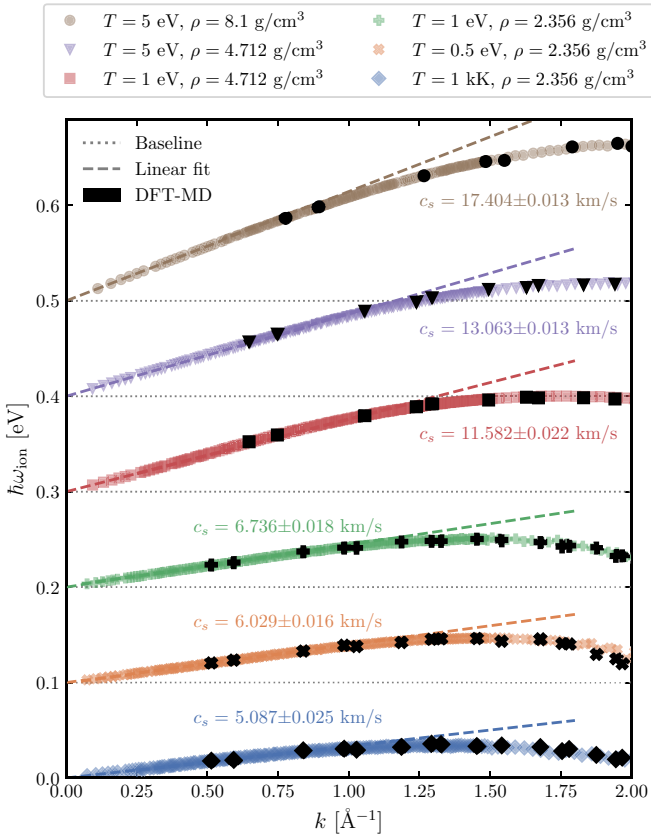

FIG. 7. Long-wavelength behavior of the oscillation frequency of the ion acoustic waves ω_{ion} as a function of the wave number k for aluminum at various conditions. The linear behavior for small k, predicted by the hydrodynamic model, is indicated by dashed lines and the inferred speed of sound is shown. The extracted peak position from the underlying DFT-MD simulations are also indicated by the black symbols. For clarity each set of curves is shifted by an offset of 0.1 eV with respect to the lower one. The dotted lines represent the baseline for each set.

ibilities χ_S and χ_T. In order to evaluate these expressions, we perform additional simulations at 5% to 10% below and above the desired density and temperature and evaluate the derivatives using central finite differences. The results are summarized in Table II. The agreement between both methods is good for all conditions that are hotter than 1000 K. At these conditions, the results for the direct calculation via (22) deviate less than 5% from the value extracted from the fit to the GCM model. However, just above the melting line at 1000 K, the direct calculation results in a prediction for the adiabatic speed of sound which is ∼10% lower than the result extracted from the fit. This speed of sound lines up better with the experimentally observed value, indicating that the hydrodynamic limit at this condition might require even smaller wave numbers than accessible in this work.

In Fig. 7, we also indicate the frequencies that we determined directly from the DFT-MD simulations (black symbols). Due to the significantly smaller simulation size, the available wave vectors cover the k axis more sparsely and the smallest available wave vectors are at least seven times larger than the smallest wave vectors from the NN-MD. The dispersion is reproduced well by the NN-MD in all cases. For the simulations at $\rho = 2.356$ g/cm^3, the lowest five k values of our DFT-MD results lie within the linear behavior of the dispersion, while the denser conditions have at most two k values in the linear regime. Therefore it would be difficult to justify a linear fit to the available DFT-MD data at these conditions.

B. Mode contributions

While fitting the DSF with one propagating and one diffusive mode is justified in the hydrodynamic limit, contributions from additional kinetic modes will become relevant at higher wave numbers. The GCM framework enables us to include arbitrary amounts of additional modes. However, the shape of the DSF is generally not discriminative enough to achieve reliable results from fitting procedures. Furthermore, statistical noise prohibits us from identifying the onset of small corrections beyond the hydrodynamic limit. In order to circumvent this limitation, we adopt the scheme laid out in Refs. [17,49,59], which uses the memory-function formalism to construct a generalized hydrodynamic matrix on an extended set of hydrodynamic variables. We employ the five-mode approach by including the first time derivatives of the longitudinal current and energy, on top of the three hydrodynamic variables. This approach does not rely on fitting to the DSF and, therefore, does not suffer from the shortcomings mentioned earlier when examining the transition to the nonhydrodynamic regime. Due to the higher memory storage demand, we only use 4000 atoms for this analysis.

In Fig. 8, we show the results of the five-mode approach compared to the three-mode approach, which can only describe generalized hydrodynamic modes, for the most extreme condition considered in this study at $T = 5$ eV and $\rho = 8.1$ g/cm^3. The other conditions show similar trends regarding the onset of nonhydrodynamic corrections. The top panel of Fig. 8 shows the decay coefficients of the various modes. In the low-k limit, only two modes tend toward zero, which identifies them as the hydrodynamic modes which will survive on long time scales. The remaining modes are two quickly decaying diffusive modes, which do not contribute in the hydrodynamic limit. At ∼0.8 Å^{-1}, the hydrodynamic and one nonhydrodynamic diffusive mode merge to create an additional propagating mode, which is the typical behavior of a damped wave equation (see Fig. 1 in Ref. [17]). The oscillation frequency of this additional mode is displayed in the bottom panel of Fig. 8. It follows the same trend as the hydrodynamic sound wave, but at a significantly lower frequency. It is apparent that these nonhydrodynamic corrections only occur for wave numbers above 0.5 Å^{-1}, but contribute significantly above 1 Å^{-1}. For smaller wave numbers, the three- and five-mode approaches give virtually the same predictions, giving credence to our fit functions (8) and (10). We, therefore, conclude that fitting to these functions at small k will in fact reveal the thermodynamic and transport properties that describe the hydrodynamic model [14].

C. Ionic transport

As mentioned in Sec. III A, the general diffusive and propagating modes from Eqs. (8) and (10) can be identified as the

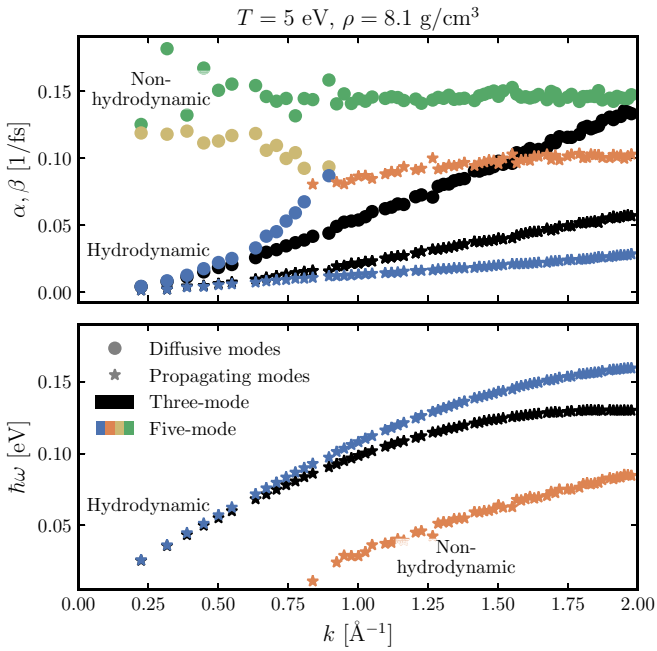

FIG. 8. Decay coefficients according to the five-mode and three-mode GCM approach (top) and frequencies of the propagating modes (bottom). Propagating modes are denoted by stars and diffusive modes by full circles, colors enumerate the different modes of the five-mode approach, while black symbols denote the generalized hydrodynamic modes of the three-mode approach.

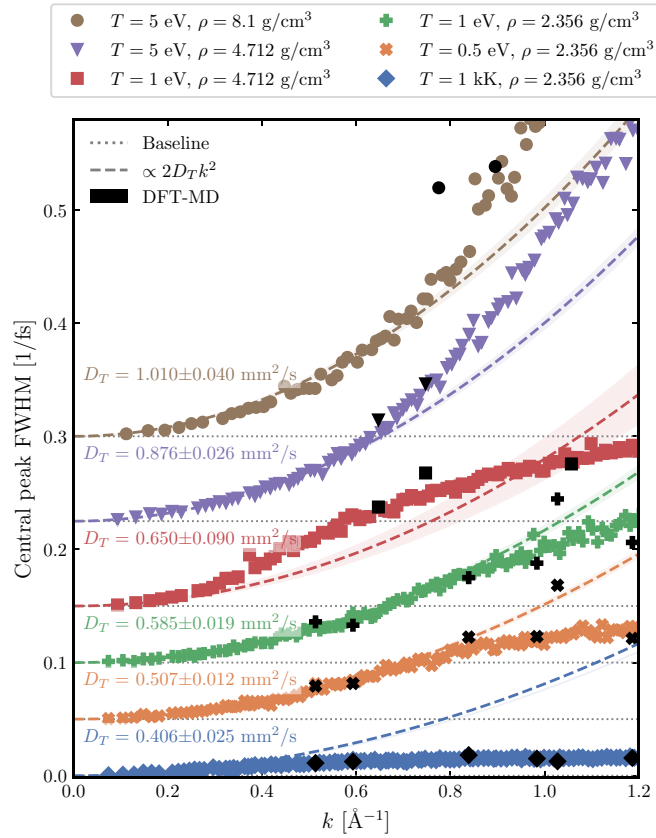

FIG. 9. FWHM of the central, diffusive peak of the DSF in equation (10), which is given by 2α, dependent on the wave number k. A fit to $2D_T k^2$ is indicated and the best fit result for the thermal diffusivity D_T is given. The extracted FWHM from the underlying DFT-MD simulations are also indicated by black symbols. For clarity, each set of curves is shifted by an offset with respect to the lower one. The dotted lines represent the baseline for each set.

well known hydrodynamic modes [21] in the limit of $k \to 0$ and $\omega \to 0$. In this limit, the diffusive mode is connected to the thermal diffusivity D_T via $\alpha = D_T k^2$ and the propagating mode becomes symmetric, i.e., B_2 vanishes, while $\beta = \Gamma k^2$, where Γ is the sound attenuation coefficient. Therefore the behavior of the decay coefficients in equation (8), which describe how fast diffusive and collective processes decay with time, can be connected to well known material properties. As these coefficients also determine the full width at half maximum (FWHM) of the peaks in the DSF [see Eq. (10)], this allows both experiment and theory to access these properties of interest, provided that the hydrodynamic regime of wave numbers is reached.

In Fig. 9, we show the FWHM of the zero-centered diffusive peak in the DSF for the considered liquid conditions. The FWHM is given by 2α, and α is found by fitting to the DSF and intermediate scattering function of the NN-MD simulations. The results that were found by fitting to the underlying DFT-MD simulations are also shown by the black symbols in Fig. 9. It is apparent that the hydrodynamic regime for this quantity is reached at lower wave numbers than for the dispersion relation in Fig. 7. None of the considered cases have more than two DFT-MD data points in the region that matches the indicated limiting behavior. Additionally, the FWHM of the central mode is sensitive to statistical fluctuations and requires a large number of time steps in order to reach converged results. Due to computational limitations, we perform 40 000 or fewer time steps for all DFT-MD simulations, while we perform between 150 000 and 600 000 time steps for the NN-MD simulations. The statistical fluctuations induced by the shorter simulations can be observed in Fig. 9.

Additionally, the lowest available wave numbers correspond to only a few wave vectors. For a cubic simulation box, only three wave vectors are averaged to compute the smallest k. For the DFT-MD simulations, only the smallest k approach the hydrodynamic limit, where only very few k vectors correspond to each k value, leading to worse statistical averages compared to the NN-MD simulations.

We follow the approach outlined in Ref. [20] to compute the thermal conductivity of the ions λ_{ii} from the thermal diffusivity D_T. We employ the thermodynamic derivatives

$$C_{\mathrm{m},V} = \left(\frac{\partial U_{\mathrm{m}}}{\partial T}\right)_V, \tag{24}$$

$$C_{\mathrm{m},P} - C_{\mathrm{m},V} = V_{\mathrm{m}}\, T \left(\frac{\partial P}{\partial T}\right)_V^2 \left(\frac{\partial V_{\mathrm{m}}}{\partial P}\right)_T \tag{25}$$

to determine the molar heat capacities at constant volume $C_{\mathrm{m},V}$ and at constant pressure $C_{\mathrm{m},P}$. The internal energy per mol is given by U_{m} and the molar volume is V_{m}. Note that if U_{m} is taken from the DFT-MD simulations, the molar heat capacities contain contributions from thermal electronic

TABLE III. Molar total heat capacity at constant volume $C_{m,V}$ and at constant pressure $C_{m,P}$ computed via thermodynamic derivatives from DFT-MD simulations for various temperatures and densities. These values include the electronic contribution. The corresponding adiabatic coefficient is also given.

T (K)	ρ (g/cm^3)	$C_{m,V}$ [J/(K mol)]	$C_{m,P}$ [J/(K mol)]	γ
1000	2.356	25.9 ± 1.9	34.2 ± 2.8	1.32 ± 0.04
5802	2.356	24.9 ± 1.0	31.4 ± 1.5	1.263 ± 0.026
11 600	2.356	29 ± 4	38 ± 5	1.30 ± 0.07
11 600	4.712	31.6 ± 3.3	35 ± 4	1.093 ± 0.017
58 020	4.712	44 ± 11	53 ± 15	1.22 ± 0.08
58 020	8.1	44 ± 8	48 ± 10	1.103 ± 0.029

excitations. These contributions can be removed by subtracting the electronic heat capacity via $C_{V,e} = T\,(\frac{\partial S_e}{\partial T})_V$, with the electronic entropy S_e. However, removing the contributions of electronic excitations from the pressure, which influences $C_{m,P}$, is not easily possible. Therefore we compute the heat capacity from the NN-MD simulations which were consistently trained on DFT-MD energies excluding the electronic excitation energy. Both procedures yield heat capacities at constant volume within 5% for the densities and temperatures considered here. We summarize the heat capacities computed from the DFT-MD simulations without the subtraction of the electronic contribution in Table III and the heat capacities computed from the NN-MD in Table IV.

The thermal conductivity of the ionic subsystem λ_{ii} can now be computed via

$$\lambda = D_T \frac{C_{m,P}}{V_m}, \tag{26}$$

results are given in Table V. In order to compare the ionic thermal conductivity extracted from the hydrodynamic limit to another approach based on the same DFT-MD simulations, we compare with the linear response treatment of the thermal conductivity as described in Ref. [60]. We have parametrized radial force fields between the ions with Eq. (6) from Ref. [60], setting the potential cutoff parameter to $C = 6$, which was sufficient to produce converged thermal conductivities. The generated force fields between the aluminum ions are purely repulsive. The ionic thermal conductivity $\lambda_{ii,GK}$ was then calculated with the Green-Kubo formula using the

TABLE IV. Molar ionic heat capacity at constant volume $C_{m,V}$ and at constant pressure $C_{m,P}$ computed via thermodynamic derivatives from NN-MD simulations for various temperatures and densities. The corresponding adiabatic coefficient is also given.

T (K)	ρ (g/cm^3)	$C_{m,V}$ [J/(K mol)]	$C_{m,P}$ [J/(K mol)]	γ
1000	2.356	24.62 ± 0.20	31.69 ± 0.29	1.287 ± 0.004
5802	2.356	18.719 ± 0.027	23.64 ± 0.04	1.2631 ± 0.0008
11 600	2.356	17.36 ± 0.09	22.11 ± 0.13	1.274 ± 0.003
11 600	4.712	23.61 ± 0.12	25.92 ± 0.14	1.0976 ± 0.0008
58 020	4.712	17.61 ± 0.15	20.67 ± 0.19	1.1736 ± 0.0027
58 020	8.1	19.83 ± 0.17	21.09 ± 0.18	1.0637 ± 0.0009

TABLE V. The thermal conductivity $\lambda_{ii,HD}$, computed from D_T in Fig. 9 via Eq. (26), and the thermal conductivity $\lambda_{ii,GK}$ computed from the Green-Kubo relation as described in Ref. [60] for aluminum at given temperatures T and mass densities ρ.

T (K)	ρ (g/cm^3)	$\lambda_{ii,HD}$ [W/(m K)]	$\lambda_{ii,GK}$ [W/(m K)]
1000	2.356	1.12 ± 0.07	0.93 ± 0.10
5802	2.356	1.05 ± 0.03	1.01 ± 0.11
11 600	2.356	1.13 ± 0.04	1.08 ± 0.11
11 600	4.712	2.9 ± 0.4	3.4 ± 0.4
58 020	4.712	3.16 ± 0.09	2.5 ± 0.6
58 020	8.1	6.40 ± 0.25	5 ± 1

ionic trajectories from the DFT-MD simulations as described in Ref. [60]. Table V contains the results, which are in good agreement with those derived from the dynamic structure factor.

For completeness, note that the total thermal conductivity of liquid metals is usually dominated by the electronic part, e.g., the experimentally observed value for liquid aluminum at 1000 K [61] is two orders of magnitude larger than the value we determined for the ionic thermal conductivity. This prevents a direct comparison of our calculated ionic thermal conductivities with experiments.

In Fig. 10, we show the FWHM of the propagating mode, which appears at the finite excitation frequency indicated in Fig. 6. From fitting to the low-k behavior of the FWHM, the longitudinal sound attenuation coefficient Γ can be determined. The statistical fluctuations in this mode are significantly smaller than in the diffusive mode, making it easier to determine where the hydrodynamic regime begins. Especially at the lowest available density $\rho = 2.356$ g/cm^3, higher temperatures lead to an extension of the hydrodynamic regime to higher wave numbers. Due to these smaller statistical fluctuations, the agreement with the significantly shorter DFT-MD simulations is also better than in the diffusive mode.

VI. CONCLUSIONS

In this work, we gave an extensive overview of the computation of the ionic DSF and intermediate scattering function and some relevant practical considerations for its application in the WDM regime. We introduced a simple GCM model with one diffusive and one propagating mode which can be matched to the dynamic behavior of liquid aluminum via a fitting procedure. We showed that liquid aluminum from the melting line up to the WDM regime can be approximated well by this simple model across all length scales apart from the distances corresponding to the first correlation peak in the static ion-ion structure factor, where the description breaks down. Good agreement with experimental data for the static and dynamic ion-ion structure factor was observed for liquid aluminum at 1000 K. We demonstrated how information about the k and ω dispersion can be extracted from the fitting procedure and highlighted the convergence to the hydrodynamic model in the limit of long wave lengths. The inability of DFT-MD simulations to reach statistically converged results in the hydrodynamic regime, due to computational limitations, was demonstrated. This shortcoming can be circumvented by

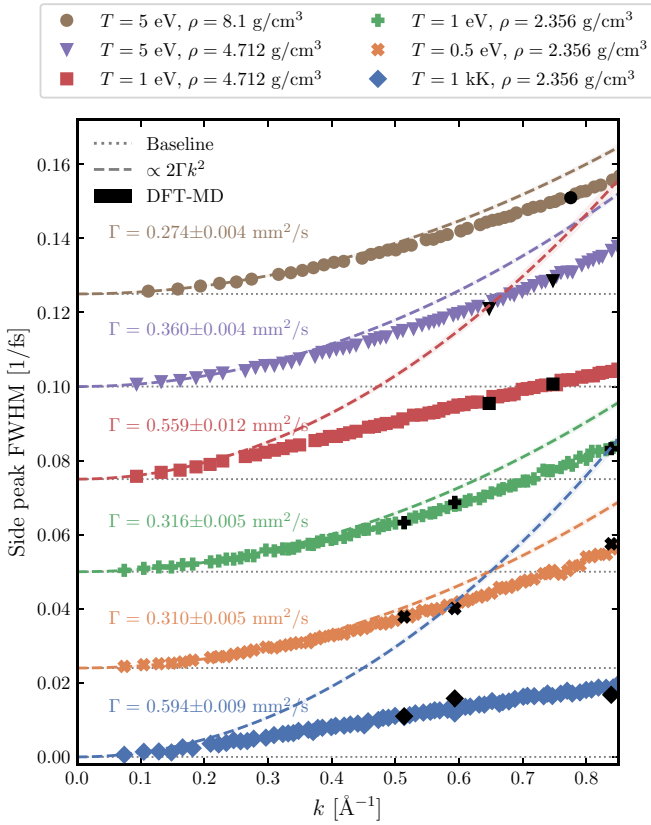

FIG. 10. FWHM of the propagating side peaks of the DSF in equation (10), which is given by 2β, dependent on the wave number k. A fit to $2\Gamma k^2$ is indicated and the best fit result for the sound attenuation coefficient Γ is given. The extracted FWHM from the underlying DFT-MD simulations are also indicated by black symbols. For clarity each set of curves is shifted by an offset with respect to the lower one. The dotted lines represent the baseline for each set.

using molecular dynamics simulations powered by a neural network trained on Behler-Parrinello symmetry functions. We showed that this procedure can be used to perform simulations with 32 000 atoms and up to 600 000 time steps. Thus this enabled us to extract thermal conductivities of the ions in the hydrodynamic limit and we compared these results with ionic thermal conductivities computed from a Green-Kubo relation. Reasonable agreement between the two approaches was observed for the considered conditions. We emphasize the importance of using only the ionic heat capacity, as opposed to the total heat capacity, to compute the ionic thermal conductivity from the ionic thermal diffusivity. We demonstrated that additional nonhydrodynamic modes do not contribute in the k range of interest, by computing a five- and three-mode GCM model and showing that they converge to the same result in the hydrodynamic limit.

The approach presented here for warm dense aluminum can be applied to other single-component materials like iron, water or hydrogen as relevant in geophysics or planetary physics. Based on corresponding simulation results for the dynamic ion-ion structure factor, combining DFT calculations and neural networks, reasonable predictions for the sound velocity, thermal diffusivity or thermal conductivity can be made for matter under extreme conditions. Perspectively, these properties will be probed experimentally using inelastic x-ray scattering (IXS) experiments at free electron laser facilities. High-resolution IXS platforms with meV-monochromators are currently implemented at the European XFEL [33,34] and the LCLS in Stanford [35]. The corresponding spectra can then be compared to, e.g., GCM models as outlined here and, if the resolution of the measured spectra is sufficient, thermal and transport properties can be extracted from the dynamical properties of WDM. Such combined efforts would improve the so far rather scarce data basis for WDM considerably and thereby enable upgraded models for the interior structure and thermal evolution of solar and extrasolar planets.

ACKNOWLEDGMENTS

We thank Th. Bornath, S. H. Glenzer, G. Gregori, W. Lorenzen, P. Neumayer, K.-U. Plagemann, T. G. White, and U. Zastrau for helpful discussions and T. G. White for providing data. We thank the anonymous referees for helpful comments. This work was supported by the North German Supercomputing Alliance (HLRN) and the ITMZ of the University of Rostock. We thank the Deutsche Forschungsgemeinschaft (DFG) for support within the Research Unit FOR 2440.

[1] W. D. Kraeft, D. Kremp, W. Ebeling, and G. Röpke, *Quantum Statistics of Charged Particle Systems* (Akademie-Verlag, Berlin, 1986).
[2] D. Kremp, M. Schlanges, and W. D. Kraeft, *Quantum Statistics of Nonideal Plasmas* (Springer, Berlin, 2004).
[3] S. Ichimaru, *Statistical Plasma Physics, Vol. II: Condensed Plasmas* (Addison Wesley, Reading, 1994).
[4] *Introduction to Computational Methods in many Body Physics*, edited by M. Bonitz and D. Semkat (Rinton Press, Berlin, 2006).
[5] T. Duffy, N. Madhusudhan, and K. K. M. Lee, in *Treatise on Geophysics*, 2nd ed., edited by G. Schubert (Elsevier, Oxford, 2015), Vol. 2, Chap. 2.07, pp. 149–178.
[6] Y. Miguel, T. Guillot, and L. Fayon, Astron. Astrophys. **596**, A114 (2016).
[7] R. Helled, G. Mazzola, and R. Redmer, Nat. Rev. Phys. **2**, 562 (2020).
[8] J. J. Fortney, M. Ikoma, N. Nettelmann, T. Guillot, and M. S. Marley, Astrophys. J. **729**, 32 (2011).
[9] J. Leconte and G. Chabrier, Astron. Astrophys. **540**, A20 (2012).
[10] G. Schubert and K. M. Söderlund, Phys. Earth Planet. Inter. **187**, 92 (2011).
[11] J. Wicht, M. French, S. Stellmach, N. Nettelmann, T. Gastine, L. Duarte, and R. Redmer, in *Magnetic Fields in the Solar System*, edited by H. Lühr, J. Wicht, S. A. Gilder, and M. Holschneider (Springer, Cham, 2018), Chap. 2, pp. 7–81.
[12] F. Graziani, M. P. Desjarlais, R. Redmer, and S. B. Trickey (editors), *Frontiers and Challenges in Warm Dense Matter* (Springer, Cham, 2014).

[13] J. M. McMahon, M. A. Morales, C. Pierleoni, and D. M. Ceperley, Rev. Mod. Phys. **84**, 1607 (2012).
[14] J. P. Hansen and I. R. McDonald, *Theory of simple liquids*, 3rd ed. (Elsevier Academic Press, London, 2006).
[15] I. M. de Schepper and E. G. D. Cohen, Phys. Rev. A **22**, 287 (1980).
[16] W. E. Alley and B. J. Alder, Phys. Rev. A **27**, 3158 (1983).
[17] I. Mryglod, Condens. Matter Phys. **1**, 753 (1998).
[18] J. P. Mithen, J. Daligault, and G. Gregori, Phys. Rev. E **83**, 015401(R) (2011).
[19] J. P. Mithen, Phys. Rev. E **89**, 013101 (2014).
[20] B. Cheng and D. Frenkel, Phys. Rev. Lett. **125**, 130602 (2020).
[21] J. P. Hansen, I. R. McDonald, and E. L. Pollock, Phys. Rev. A **11**, 1025 (1975).
[22] I. Morozov, H. Reinholz, G. Röpke, A. Wierling, and G. Zwicknagel, Phys. Rev. E **71**, 066408 (2005).
[23] T. G. White, S. Richardson, B. J. B. Crowley, L. K. Pattison, J. W. O. Harris, and G. Gregori, Phys. Rev. Lett. **111**, 175002 (2013).
[24] H. R. Rüter and R. Redmer, Phys. Rev. Lett. **112**, 145007 (2014).
[25] B. B. L. Witte, M. Shihab, S. H. Glenzer, and R. Redmer, Phys. Rev. B **95**, 144105 (2017).
[26] Q. Zeng, X. Yu, Y. Yao, T. Gao, B. Chen, S. Zhang, D. Kang, H. Wang, and J. Dai, Phys. Rev. Research **3**, 033116 (2021).
[27] L. Harbour, G. D. Förster, M. W. C. Dharma-wardana, and L. J. Lewis, Phys. Rev. E **97**, 043210 (2018).
[28] J. Clérouin, N. Desbiens, V. Dubois, and P. Arnault, Phys. Rev. E **94**, 061202(R) (2016).
[29] T. Morawietz, A. Singraber, C. Dellago, and J. Behler, Proc. Natl. Acad. Sci. USA **113**, 8368 (2016).
[30] A. Singraber, T. Morawietz, J. Behler, and C. Dellago, J. Chem. Theory Comput. **15**, 3075 (2019).
[31] A. Singraber, n2p2 - a neural network potential package, https://zenodo.org/record/4750573.
[32] J. Behler and M. Parrinello, Phys. Rev. Lett. **98**, 146401 (2007).
[33] A. Descamps, B. K. Ofori-Okai, K. Appel, V. Cerantola, A. Comley, J. H. Eggert, L. B. Fletcher, D. O. Gericke, S. Göde, O. Humphries, O. Karnbach, A. Lazicki, R. Loetzsch, D. McGonegle, C. A. J. Palmer, C. Plueckthun, T. R. Preston, R. Redmer, D. G. Senesky, C. Strohm *et al.*, Sci. Rep. **10**, 14564 (2020).
[34] L. Wollenweber, T. R. Preston, A. Descamps, V. Cerantola, A. Comley, J. H. Eggert, L. B. Fletcher, G. Geloni, D. O. Gericke, S. H. Glenzer, S. Göde, J. Hastings, O. S. Humphries, A. Jenei, O. Karnbach, Z. Konopkova, R. Loetzsch, B. Marx-Glowna, E. E. McBride, D. McGonegle *et al.*, Rev. Sci. Instrum. **92**, 013101 (2021).
[35] E. E. McBride, T. G. White, A. Descamps, L. B. Fletcher, K. Appel, F. P. Condamine, C. B. Curry, F. Dallari, S. Funk, E. Galtier, M. Gauthier, S. Goede, J. B. Kim, H. J. Lee, B. K. Ofori-Okai, M. Oliver, A. Rigby, C. Schoenwaelder, P. Sun, T. Tschentscher *et al.*, Rev. Sci. Instrum. **89**, 10F104 (2018).
[36] G. Kresse and J. Hafner, Phys. Rev. B **47**, 558 (1993).
[37] G. Kresse and J. Hafner, Phys. Rev. B **49**, 14251 (1994).
[38] G. Kresse and J. Furthmüller, Phys. Rev. B **54**, 11169 (1996).
[39] N. D. Mermin, Phys. Rev. **137**, A1441 (1965).
[40] J. P. Perdew, K. Burke, and M. Ernzerhof, Phys. Rev. Lett. **77**, 3865 (1996).
[41] P. E. Blöchl, Phys. Rev. B **50**, 17953 (1994).
[42] S. Nosé, J. Chem. Phys. **81**, 511 (1984).
[43] W. G. Hoover, Phys. Rev. A **31**, 1695 (1985).
[44] A. Baldereschi, Phys. Rev. B **7**, 5212 (1973).
[45] G. Kresse and J. Furthmüller, Comput. Mater. Sci. **6**, 15 (1996).
[46] M. Gastegger, L. Schwiedrzik, M. Bittermann, F. Berzsenyi, and P. Marquetand, J. Chem. Phys. **148**, 241709 (2018).
[47] A. P. Thompson, H. M. Aktulga, R. Berger, D. S. Bolintineanu, W. M. Brown, P. S. Crozier, P. J. in 't Veld, A. Kohlmeyer, S. G. Moore, T. D. Nguyen, R. Shan, M. J. Stevens, J. Tranchida, C. Trott, and S. J. Plimpton, Comput. Phys. Commun. **271**, 108171 (2022).
[48] T. Bryk and A. B. Belonoshko, Phys. Rev. B **86**, 024202 (2012).
[49] T. Bryk, Eur. Phys. J. Spec. Top. **196**, 65 (2011).
[50] J.-F. Wax and T. Bryk, J. Phys.: Condens. Matter **25**, 325104 (2013).
[51] P. Virtanen *et al.*, Nature Methods **17**, 261 (2020).
[52] P. D. Welch, IEEE Trans. Audio Electroacoust. **15**, 70 (1967).
[53] Y. Waseda, *The Structure of Non-Crystalline Materials* (McGraw-Hill, New York, 1980).
[54] T. Scopigno, U. Balucani, G. Ruocco, and F. Sette, Phys. Rev. E **63**, 011210 (2000).
[55] M. M. G. Alemany, L. J. Gallego, and D. J. González, Phys. Rev. B **70**, 134206 (2004).
[56] P. G. De Gennes, Physica **25**, 825 (1959).
[57] S. Blairs, Int. Mater. Rev. **52**, 321 (2007).
[58] J. Schnakenberg, *Thermodynamik und Statistische Physik*, 1st ed. (Wiley, Hoboken, NJ, 1998).
[59] I. Mryglod, I. Omelyan, and M. Tokarchuk, Mol. Phys. **84**, 235 (1995).
[60] M. French, New J. Phys. **21**, 023007 (2019).
[61] M. Leitner, T. Leitner, A. Schmon, K. Aziz, and G. Pottlacher, Metall. Mater. Trans. A **48**, 3036 (2017).